HHS Public Access

Author manuscript

*IEEE Trans Ultrason Ferroelectr Freq Control*. Author manuscript; available in PMC 2016 November 01.

Published in final edited form as:

*IEEE Trans Ultrason Ferroelectr Freq Control*. 2015 November ; 62(11): 1913–1927. doi:10.1109/TUFFC.2015.007004.

# A Model and Regularization Scheme for Ultrasonic Beamforming Clutter Reduction

**Brett Byram [Member, IEEE]**, **Kazuyuki Dei [Student Member, IEEE]**, **Jaime Tierney**, and **Douglas Dumont [Member, IEEE]**

Department of Biomedical Engineering at Vanderbilt University, Nashville, TN 27708, USA

## Abstract

Acoustic clutter produced by off-axis and multipath scattering is known to cause image degradation, and in some cases these sources may be the prime determinants of *in vivo* image quality. We have previously shown some success addressing these sources of image degradation by modeling the aperture domain signal from different sources of clutter, and then decomposing aperture domain data using the modeled sources. Our previous model had some shortcomings including model mismatch and failure to recover B-Mode speckle statistics. These shortcomings are addressed here by developing a better model and by using a general regularization approach appropriate for the model and data. We present results with L1 (lasso), L2 (ridge), and L1/L2 combined (elastic-net) regularization methods. We call our new method aperture domain model image reconstruction (ADMIRE). Our results demonstrate that ADMIRE with L1 regularization, or weighted toward L1 in the case of elastic-net regularization, have improved image quality. L1 by itself works well, but additional improvements are seen with elastic-net regularization over the pure L1 constraint. On *in vivo* example cases, L1 regularization showed mean contrast improvements of 4.6 and 6.8 dB on fundamental and harmonic images, respectively. Elastic net regularization ($a = 0.9$) showed mean contrast improvements of 17.8 dB on fundamental images and 11.8 dB on harmonic images. We also demonstrate that in uncluttered Field II simulations the decluttering algorithm produces the same contrast, contrast-to-noise ratio, and speckle SNR as normal B-mode imaging, demonstrating that ADMIRE preserves typical image features.

## I. Introduction

Ultrasound's low-cost and convenience make it the most widely used advanced clinical imaging modality in the United States [1]. Unfortunately, ultrasound's broad utility belies its quality in many real clinical instances in which most exams are subjected to at least some level of image degradation and many fail altogether [2–6]. Often poor image-quality is attributable to penetration and resolution limitations, but acoustic clutter may be the most significant and widespread cause of image degradation [7].

Acoustic clutter is something of a catch-all term for non-diffraction limited image degradation, which includes multipath scattering, off-axis scattering, and phase-aberration induced degradation of the point spread function. Several methods have been proposed to

(brett.c.byram@vanderbilt.edu).

suppress these sources of degradation including correcting temporal wavefront distortions (e.g., phase-aberration correction [8–10], standard and adaptive apodization schemes [11–15], and harmonic imaging [16–18]). With the exception of harmonic imaging, these techniques have had only mixed clinical success.

Although most beamforming methods in the literature have focused on restoring, optimizing, or surpassing diffraction limited beamforming, suppressing multipath scattering has also been explored. Several methods exist, but again harmonic imaging is the most clinically impactful [7], [17,18], although it still does not eliminate all clutter [19]. Time reversal is a classic method for suppressing multipath scattering if a point target or a rapidly changing speckle pattern are available [20,21], but it is harder to apply to attenuating media [22]. There are also several new methods that suppress multipath clutter. One new method is second-order ultrasound field (SURF) imaging, which takes advantage of nonlinear wave propagation by directly manipulating nonlinear propagation in a way that specifically targets the multipath scattering problem [19], [23–25]. SURF imaging is promising, but it may be some time before the necessary high-bandwidth transducers and arbitrary transmitters are readily available [19]. A second set of new methods are the aperture domain coherence-based beamformers, which include short-lag spatial coherence imaging [26–29]. These methods suppress off-axis and multipath scattering and have translated very well to *in vivo* scenarios. Their biggest challenge may be that they create fundamentally different images compared with normal B-mode images, which may hinder clinical adoption. Aperture domain coherence methods also eliminate the RF signal, making them unsuitable for estimating displacement using conventional high-quality methods.

To address the problem of both multipath and off-axis clutter sources, we recently proposed a new model-based approach [30]. The primary goal of the approach is to preserve the ultrasound channel data (or RF data), while minimizing acoustic clutter. A secondary goal is to develop a tool that can characterize the spatial distribution of clutter from *in vivo* data. The method relies on linearizing the problem of multipath scattering by ignoring multipath propagation and considering multiple scattering as time-delayed wavefronts arriving from depths shallow to the normal region of interest. The initial model of this linearization applied the Fresnel approximation so that the signal sampled by a transducer array could be modeled as a summation of linear frequency modulated sinusoids,

$$p_s(x;t,\omega) \approx \sum_{n=0}^{N-1} A_n e^{jg_n x^2 + jk_n x + j\phi_n}, \quad (1)$$

where

$$g_n = \frac{kz_n}{2z_f(z_f - z_n)}, \quad \text{and} \quad k_n = \frac{-x_n k}{z_f - z_n},$$

and where each $N$ is a scattering source at location ($x_n$, $z_n$) encoded by the chirp-rates, $g_n$, and frequencies, $k_n$. $z_f$ is the depth of the signal of interest, and $k$ is the wavenumber. By using this model to decompose a signal into its scattering sites and reconstructing only the signals from the region of interest, we demonstrated image quality improvements.

Specifically, the method demonstrated significant improvements in contrast, but little change in contrast-to-noise ratio (CNR) on average. This seemingly paradoxical result was probably caused by the lower speckle SNR compared with normal B-mode imaging. To address these shortcomings and several open questions from the previous work, we present a new model and decomposition scheme, which we call aperture domain model image reconstruction (ADMIRE).

## II. Methods

### A. Received Wavefront Model

In our previous model, we made several approximations so that our model components were constant amplitude, linear-frequency-modulated sinusoids. The previous simplifications are ignored here, and the new model for ADMIRE incorporates

- the exact wavefront delay profile,
- the effect of dynamic receive beamforming on multipath sources,
- the impact of the axial short-time Fourier transform (STFT) window, and
- element directional sensitivity.

The model incorporating these effects can be presented generically as

$$p_s(x;t,\omega) = \sum_{n=0}^{N-1} A(x;x_n, z_n, \tau_n, \omega)\, e^{jk\tau(x;x_n,z_n,\tau_n)}, \quad (2)$$

where $k$ is the wavenumber, $x$ is the aperture position, $t$ and $\omega$ localize the signal in time and frequency, $\tau(x; x_n, z_n, \tau_n)$ is the wavefront delay for a signal arriving from point $(x_n, z_n)$ at time $\tau_n$ and $A(x; x_n, z_n, \tau_n, \omega)$ is the lateral amplitude modulation induced by the STFT and the element sensitivity. $A(x; x_n, z_n, \tau_n, \omega)$ also depends on the signal's pulse shape and $\tau(x, x_n, z_n, \tau_n)$.

The new model produces similar predictors as (1) but is no longer restricted to producing just linear, frequency-modulated sinusoids. Before proceeding with a description of the various components of the model, several example wavefronts are shown in Fig. 1. The figure qualitatively compares new and old models against Field II simulated data to provide additional intuition and motivation for the new model.

To establish the specifics of (2), we first consider a scattered wavefront's arrival-time profile. For the typical free-space diffraction case, this is

$$\tau_{Diff}(x;x_n, z_n, \tau_n) = \frac{1}{c}\sqrt{(x - x_n)^2 + z_n^2} + \tau_{n_0}. \quad (3)$$

Usually, $\tau_{n0}$ would be defined as $z_n/c$, which models a ballistic wave propagating directly to the region of interest, scattering, and then propagating directly back to the array. However, $\tau_{n0}$ is more general in our linearized representation of multipath scattering. In our representation, $\tau_{n0}$ can be any value within the receive duration of the ultrasound system, but

practically, its value is limited based on the axial STFT window and the curvature for a given depth. We find it more convenient to define $\tau_{n_0} = (1/c)(2z_f - z_n) + \tau_n$, and then parameterize the model space using $\tau_n$.

Modeling the wavefront curvature from a given source location is straightforward and consistent with our previous approach. Here, we also introduce the impact of dynamic receive delays on the modeled wavefronts. In principal, applying dynamic receive delays is not necessary, but dynamically delaying the wavefronts and modeling this process has at least one clear benefit and another possible benefit. First, dynamic receive delays flatten the curvature of all wavefronts, including wavefronts resulting from multiple scattering. A flatter curvature means a wider segment of that wavefront falls within a given STFT window allowing for better estimation resolution. Second, dynamically delaying the wavefronts provides an opportunity to advantageously modulate the aperture domain signal to help better preserve the signal of interest.[1]

First, we consider the impact of applying dynamic receive delays to wavefronts originating from multipath scattering. The problem is that wavefronts arriving from depths besides the intended focus have different curvatures than the corresponding receive delay profiles, and therefore these multiply scattered wavefronts traverse several different dynamic receive profiles, as illustrated in Fig. 2. To model this effect, the perceived depth of each part of the sampled wavefront needs to be computed so that the correct delays can be used in (2). To accomplish this, we start with the usual dynamic receive delays across the aperture and through depth

$$\tau_{DR}(x;x_f,z_f) = \frac{1}{c}\sqrt{(x-x_f)^2+z_f^2} + \frac{z_f}{c}, \quad (4)$$

where $x$ is the aperture location and $(x_f, z_f)$ are the dynamically updated focal locations. Next, we equate the multipath wavefront delays and the dynamic receive delays

$$\tau_{Diff}(x;x_n,z_n,\tau_n) = \tau_{DR}(x;x_f,z_f) \quad (5)$$

and solve for $z_f$. Purely by rearrangement, the result is

$$z_f(x) = \frac{d_0(x)^2 - (x_f - x)^2}{2d_0(x)}, \quad (6)$$

where

$$d_0(x) = \sqrt{(x-x_n)^2+z_n^2} + c\tau_{n_0}.$$

[1]This is consistent with concepts in spectral estimation where the Cramer-Rao lower bound for a given frequency estimate is a function of that frequency [31]. Of note here is that for spectral estimation problems the Cramer-Rao bound for the dc estimation variance is incredibly poor. In the application considered here without an additional modulation, the wavefronts from the region of interest will be nearly dc signals.

Finally, the value for $z_f(x)$ can be inserted back into (4) to calculate the dynamic receive delay applied across each multiply scattered wavefront.

Next, we describe a method for intentionally modulating the aperture domain signal so that the primary region of interest is not near dc. The approach scales the depth dimension used for calculating the dynamic receive delay profile, which causes different receive delays than usual to be applied at a given depth. In this case, (4) is modified to

$$\tau_{DR_\gamma}(x;x_f,z_f)=\frac{1}{c}\sqrt{(x-x_f)^2+((1+\gamma)z_f)^2}+\frac{(1-\gamma)z_f}{c}, \quad (7)$$

and to extend to the multipath wavefront we again solve for $z_f(x)$ using (5) to obtain

$$z_f(x)=\frac{d_0(x)(1-\gamma)}{4\gamma}\times\left(1+sgn(\gamma)\sqrt{1-4\frac{\gamma\left((x-x_n)^2-d_0(x)^2\right)}{d_0(x)^2(1-\gamma)^2}}\right), \quad (8)$$

where $\gamma$ is the scaling factor for the depth. As defined, negative $\gamma$ creates curvatures corresponding to depths shallow to the usual focus, and the reverse for positive $\gamma$. Examples of the impact for several $\gamma$ values on wavefront curvature are shown in Fig. 3.

The wavefront delays used in (2) are

$$\tau(x;x_n,z_n,\tau_n)=\tau_{Diff}(x;x_n,z_n,\tau_n)-\tau_{DR}(x;x_f,z_f(x))-(1+\gamma)\frac{z_f(x)}{c}. \quad (9)$$

The wavefront delay is important for establishing the signal's phase across the aperture, but it is also important for calculating the amplitude modulation, $A(x)$, across the aperture. Using the modeled delay and an estimate of the pulse shape the lateral amplitude modulation can be calculated as

$$A_{FT}^2(x)=\int_{t_c-(\Delta t/2)}^{t_c+(\Delta t/2)} w_{FT}^2(t-t_c)\,w_{env}^2(t-\tau(x;x_n,z_n,\tau_n))\,\mathrm{d}t, \quad (10)$$

where $\Delta t$ is the width of the STFT window, $t_c$ is the center of the STFT window, $w_{\mathrm{FT}}$ is the window used for the STFT, and $w_{\mathrm{env}}$ is the axial pulse envelope. For many relevant cases of $w_{\mathrm{FT}}$ and $w_{\mathrm{env}}$, $A_{\mathrm{FT}}(x)$ can be calculated analytically, but it is also possible to calculate $A_{\mathrm{FT}}(x)$ from sampled realizations of $w_{\mathrm{FT}}$ and $w_{\mathrm{env}}$. This second case may be useful for more exact representations of the pulse shape using empirical hydrophone measurements, or to adaptively estimate the pulse shape based on speckle statistics [32]. Here, for simplicity, we restrict ourselves to a rectangular window for $w_{\mathrm{FT}}$ and a Gaussian envelope for $w_{\mathrm{env}}$. This lateral modulation resulting from STFT windowing does not describe all of the potential amplitude variation across the aperture.

We also include the effect of element sensitivity as described by Selfridge *et al*. and expressed as

$$A_{es}(x) = \frac{sin\left(\frac{\pi w sin(\theta)}{\lambda}\right)}{\frac{\pi w sin(\theta)}{\lambda}} cos(\theta), \quad (11)$$

where $\theta = \tan^{-1}((x - x_n)/z_n)$ [33]. Incorporating angular sensitivity is most important for shallow scatterers with high incidence angles of the received wavefront with transducer elements. Combining angular sensitivity with the STFT characteristics gives the amplitude modulation modeled here,

$$A_n(x) = A_{FT}(x) A_{es}(x). \quad (12)$$

The accuracy of the model was determined using Field II simulations with the parameters in Table I.

## B. Model Space

Using our linearized scattering model for ADMIRE, we can express the signal received at a specific time as

$$y = X\beta, \quad (13)$$

where $y$ is a single frequency of the observed channel data from a given STFT window location constructed as

$$y = [\Re\{S_w(x_i; mT, \omega_p)\} \Im\{S_w(x_i; mT, \omega_p)\}]^T,$$

$X$ is the model matrix of predictors constructed from (2),

$$X = \begin{bmatrix} \Re\{p_s(x;t,\omega)\}^T & -\Im\{p_s(x;t,\omega)\}^T \\ \Im\{p_s(x;t,\omega)\}^T & \Re\{p_s(x;t,\omega)\}^T \end{bmatrix},$$

and $\beta$ contains the coefficients for the predictors in $X$. $\Re$ and $\Im$ denote the real and imaginary parts, respectively. The model matrix is formed by sampling the space from which scatterers are expected to return. There are many possible approaches to sampling the model space. Here, we identify a region ahead of time that will be the acceptance zone. Scatterers originating from within this zone will be used to reconstruct decluttered data, whereas scatterers outside this zone are discarded. In our experiments so far, it is most efficient to sample the model space finely within the region of acceptance and sample the model more coarsely in the rejection zone.

We define the acceptance zone based on the expected resolution of a model predictor centered in the region of interest. The lateral resolution is calculated based on the bandwidth of the signal originating from the center of the region of interest, i.e., $res_{lat} \approx \lambda z \mathcal{F}\{|p_s(x; x_c, z_c, 0)|\}_{BW}$, where $F\{|\cdot|\}_{BW}$ denotes the lateral bandwidth of the model predictor and $(x_c, z_c)$ denotes the center of the region of interest. The axial resolution of the region of interest is approximated as $res_{axl} \approx 2res_{lat}$, and comes from work on

parameter estimation of linear frequency modulated sinusoids [34]. The lateral and axial resolution are used to define an ellipsoidal acceptance region,

$$\left(\frac{x_n - x_r}{c_{\mathrm{l}} res_{lat}}\right)^2 + \left(\frac{z_n - z_r}{c_{\mathrm{a}} res_{axl}}\right)^2 \leq 1, \quad (14)$$

where $c_{\mathrm{l}}$ and $c_{\mathrm{a}}$ are scale factors selected to modify the size of the acceptance region, and $x_r$ and $z_r$ denote the center of the acceptance zone.

The sampling of the continuous parameter space of the ultrasound field can have a large outcome on the resulting decomposition. It is computationally advantageous to restrict the number of predictors in the model $X$, but an insufficiently populated model inhibits the ability of the model to suppress clutter and preserve the signal of interest. For all of the results here, we have two different sampling grids depending on whether intentional receive modulation is used. For both sampling grids, the phase parameter $\tau_n$ is the same with a spacing of $0.0485\lambda$ in the acceptance region and $0.2423\lambda$ outside the acceptance zone. For the case of normal receive delays ($\gamma = 0$), the lateral and axial grid sampling inside the acceptance zone is $0.0668\mathrm{res}_{\mathrm{lat}}$ and $0.267\mathrm{res}_{\mathrm{axl}}$, respectively, and the sampling outside the acceptance zone is $1.34\mathrm{res}_{\mathrm{lat}}$ and $1.34\mathrm{res}_{\mathrm{axl}}$, respectively. For the case of receive modulation with $\gamma = 0.5$, the sampling is finer. In this case the lateral and axial grid sampling within the acceptance region is $0.025\mathrm{res}_{\mathrm{lat}}$ and $0.10\mathrm{res}_{\mathrm{axl}}$, respectively. Outside the acceptance region, the grid sampling is $0.5\mathrm{res}_{\mathrm{lat}}$ and $0.5\mathrm{res}_{\mathrm{axl}}$, respectively. For the purposes of image reconstruction, a fixed grid is used throughout the image. This has the advantage of efficiency at the cost of increased decomposition error. For some applications not presented here, it may be desirable to incorporate model selection and regularization tuning into a more robust cross-validation scheme, which is beyond the scope of this paper.

### C. Decomposition and Regularization

Depending on the specific model-space sampling, the imaging sequence, and the imaging depth, the ADMIRE model matrix could contain anywhere from several hundred predictors to over a million predictors. This is in contrast to the number of samples in the data vector, $y$, which will rarely have more than 256 elements for a 1-D array. The massive difference between the number of data points and the number of model predictors presents a challenge. Ideally, estimating $\beta$ could be accomplished by minimizing the squared error:

$\hat{\beta} = \left(X^{\mathrm{T}} X\right)^{-1} X^{\mathrm{T}} y$, but this is ill-posed. To address this problem, additional constraints must be added in the form of regularization terms. Regularization schemes constraining the solution with L1 or L2 norms are typical. L1 is useful because it promotes coefficient sparsity, but the final solution will have fewer nonzero predictors than observations, and the predictors will be nearly (if not totally) uncorrelated. This property of L1 regularized model-fitting may be problematic for some *in vivo* ultrasound aperture-domain data sets because in many cases it will require multiple correlated model-predictors to reconstruct all scattering sources. Besides L1, the other typical scheme is L2 regularized model fitting. L2 is attractive because it allows for solutions with correlated model predictors, but whereas correlated predictors are useful, L2 performs coefficient shrinkage (not selection), so an L2 constrained solution may not have any coefficients equal to zero. Practically, this means that when using

an L2 constraint for data originating from inside an anechoic cyst (i.e., no expected scattering from within the cyst), the model fit will almost always predict that there is scattering originating from the region of interest.

L1 and L2 regularization both have shortcomings for the decomposition problem posed here. These shortcomings will be demonstrated empirically in the results. To overcome these, we use elastic-net regularization to perform the ADMIRE decomposition [35]. Elastic net regularization solves the following optimization problem,

$$\hat{\beta}=arg\ \min_{\beta}\left(\| y-X\beta \|^2+\lambda\left(\alpha\| \beta \|_1+(1-\alpha)\| \beta \|_2^2/2\right)\right), \quad (15)$$

where $\| \beta \|_1=\sum_{n=0}^{N}|\beta_n|$ is the L1 term, $\| \beta \|_2=\sqrt{\sum_{n=0}^{N}|\beta_n|^2}$ is the L2 term, $a$ is between 0 and 1 and determines the relative weight between L1 and L2, and $\lambda$ is the total regularization parameter. Elastic net regularization is attractive because it allows for correlated model predictors to be present simultaneously due to L2, but it also allows for nonzero model predictors due to the L1 term. These regularization schemes tends to introduce related sets of correlated model components as a cluster, which has been referred to as group selection. Elastic net regularization becomes an L1 problem if $a$ = 1 and L2 if $a$ = 0. The elastic net and the limiting L1 and L2 regularization problems are solved using the efficient software package glmnet [36].

To appropriately compare models with different $a$ and $\lambda$ values, it is useful to know the degrees of freedom for a given model. The general degrees of freedom for an elastic net regularized regression solution is

$$\mathrm{d}f\,(\lambda)=Tr\left[X_{\mathscr{A}}\left(X_{\mathscr{A}}^{\mathrm{T}}X_{\mathscr{A}}+\lambda I\right)^{-1}X_{\mathscr{A}}^{\mathrm{T}}\right]=\sum_{n=0}^{P-1}\frac{d_n^2}{d_n^2+\lambda}, \quad (16)$$

where $X_{\mathscr{A}}$ is a reduced model composed of only predictors with nonzero coefficient estimates and $d_n$ values are singular values of the reduced model [37]. The singular value decomposition was performed iteratively using an efficient memory approach to accommodate the potential for large model matrices [38].

### D. Signal Reconstruction

Once the signal has been spatially decomposed using the model, the final step in ADMIRE is to reconstruct a clean signal. This is accomplished by identifying model predictors within the region of interest specified by (14), which we denote as $X_{\mathscr{B}}$. The signal from the region of interest is reconstructed as

$$y_{ROI}=X_{\mathscr{B}}\hat{\beta}_{\mathscr{B}}. \quad (17)$$

The clutter suppressed signals are converted back to time-domain channel data using an inverse short-time Fourier transform (ISTFT).

### E. Short-Time Fourier Transform

The STFT used here is implemented as

$$S_i(mT, \omega_p) = \sum_{l=-\infty}^{\infty} s(l)\, w_{FT}(mT - l)\, e^{-j\omega_p l}, \quad (18)$$

where $T$ denotes the time sampling period of the STFT, $w_{\mathrm{FT}}(l)$ is the sliding window that selects the short-time segments, and $\omega_p$ are the discrete frequencies, typically distributed as $2\pi k/N$ for $k = [0,\ldots N-1]$. To make the connection back to the model clear, $S_i(mT, \omega_p)$ would be the STFT for a single channel of the aperture, where each channel is indexed by $i$, and this index corresponds to $x$ in $p_s(x; t, \omega)$.

An ISTFT is used to reconstruct the time-domain signal after the model decomposition and aperture domain signal reconstruction. The inverse transformation back into the original domain is accomplished using the least-squares ISTFT described by Yang [39], which is

$$s_i(n) = \frac{w_{FT}(mT - l) \sum_{w_p=-\infty}^{\infty} S_i(mT, \omega_p)\, e^{j\omega_p l}}{\sum_{l=-\infty}^{\infty} w_{FT}(mT - l)^2}. \quad (19)$$

### F. Computational Complexity

Signal decomposition using elastic net regularization has a computational order of $\mathcal{O}\left(m^3 + sm^2\right)$, where $s$ is the number of predictors in the model matrix, $X$, and $m$ is the number of steps in the L1 portion of the model fit [35]. (The computational complexity matches the complexity for a single ordinary least squares fit.)

### G. Multipath Simulations for Regularization Tuning

The ADMIRE model fit described by (15) requires two different regularization parameters to be empirically determined, $\alpha$ and $\lambda$. These parameters are the total regularization weight ($\lambda$) and the balance between L1 and L2 ($\alpha$). The tuning problem here is slightly different from conventional tuning problems because for imaging applications we are most interested in the error from only part of our signal, which is the signal returning from the region of interest. That is, after solving the elastic-net regularized optimization problem in (15), we obtain a set of non-zero predictors $X_{\mathscr{A}}$, and of these predictors, some additionally reduced set $X_{\mathscr{B}}$ will represent scatterers within the region of interest that will form the reconstructed signal. For imaging, the primary goal is to minimize the error of the signal of interest while maximizing suppression of energy originating outside of the acceptance zone. The error of the signal of interest is described as

$$err_{ROI} = \| y_{ROI} - X_{\mathscr{B}} \hat{\beta}_{\mathscr{B}} \|^2, \quad (20)$$

where $y_{\mathrm{ROI}}$ is the wavefront formed by scattering only from the region of interest, and $\beta_{\mathscr{B}}$ are the coefficients corresponding to the predictors within the ROI. To estimate the

reconstruction error, $\mathrm{err}_{\mathrm{ROI}}$, it is necessary to know the true wavefront of interest. The true wavefront is not knowable when using *in vivo* data, and using fully nonlinear simulations can also make knowing the true signal of interest difficult. Therefore, for model validation, basic image evaluation, and regularization tuning, we propose a pseudo-nonlinear approach to simulating multipath scattering induced signal corruption using the linear simulation package Field II [40], [41]. Field II already naturally simulates off-axis scattering and scattering from a specified region of interest, which means that once we introduce our extension, Field II can simulate all the degradation mechanisms of interest here.

To add our multipath Field II extension, we simulate multipath scattering by simulating channel data for scatterers arriving from a particular depth without any receive beamforming. We then shift the data to a later time by zero-padding and interpolating the data in the time domain to a specific time of interest. Once the multipath signals are simulated and delayed they are added to the signal of interest. The channel data from multipath scattering can be scaled to simulate various levels of clutter.

This approach allows for simulations with both off-axis and multipath clutter sources that are known exactly. For example, clutter from many different regions can be simulated, and then the amplitude of all of these clutter signals can be normalized relative to the signal of interest to create clutter with known power. Additionally, clutter from discrete scatterers can be simulated, or clutter from diffuse scatterer sites can be used to create a more complex and possibly more realistic clutter signal. Currently, each lateral line location is treated separately, which means that the lateral correlation does not mimic the expected behavior. In principle this can be accounted for, but we do not address this at this point because our algorithm is not affected by lateral correlation.

The motivation for this pseudo-nonlinear simulation approach was to easily calculate $\mathrm{err}_{\mathrm{ROI}}$, but the simulation scheme also allows for a simple contrast metric and provides more insight into regularization tuning. The contrast metric is calculated from clutter data with and without a signal of interest. This correlates to estimating the contrast of an anechoic cyst. The signal that contains both clutter and a signal of interest represents the background feature, and the signal with only clutter represents an anechoic lesion feature. The metric is calculated using

$$C_{reg}=20log_{10}\frac{w^{\mathrm{H}}\left(X_{\mathscr{B}}\hat{\beta}_{\mathscr{B}}\right)_{\text{clutter only simulation}}}{w^{\mathrm{H}}\left(X_{\mathscr{B}}\hat{\beta}_{\mathscr{B}}\right)_{\text{signal and clutter simulation}}}, \quad (21)$$

where $w$ is a beamforming vector that corrects for intentional modulation before summing and $H$ is the complex transpose. This metric provides insight into how well the signal of interest's power is preserved compared with how well the power of the clutter is suppressed.

## H. Field II Contrast Simulations

In addition to using Field II to help tune the regularization parameters, Field II is also used to evaluate the performance of ADMIRE on linear simulations of contrast phantoms. The motivation is to determine how well the decomposition algorithm preserves contrast and

contrast-to-noise ratio (CNR) in uncluttered data. This is important because in our previous model and decomposition scheme CNR was reduced in about half of the data; however, because most of the previous analysis was performed on *in vivo* data, the exact cause of the CNR decrease was impossible to determine because decreases in CNR could be due to increased structure such as blood vessels exposed in the background region. To address this, several Field II simulation experiments were conducted using the parameters in Table I. Contrast phantoms were simulated with lesion contrasts of totally anechoic, −20, −10, −5, 5, 10, and 20 dB. Each contrast level was simulated with 12 independent speckle realizations. For each data set, we measured the contrast as

$$\mathrm{C} = -20 log_{10}\left(\frac{\mu_{\mathrm{lesion}}}{\mu_{\mathrm{background}}}\right), \quad (22)$$

the CNR as

$$CNR = 20 log_{10}\left(\frac{|\mu_{\mathrm{background}} - \mu_{\mathrm{lesion}}|}{\sqrt{\sigma^2_{\mathrm{background}} + \sigma^2_{\mathrm{lesion}}}}\right), \quad (23)$$

and the speckle SNR as

$$SNR_{\mathrm{speckle}} = \frac{\mu_{\mathrm{background}}}{\sigma_{\mathrm{background}}}, \quad (24)$$

where $\mu$ and $\sigma^2$ denote the indicated mean and variance, respectively, of the enveloped but uncompressed regions of the image data.

Field II was also used to simulate cluttered contrast phantoms. In this case anechoic lesions were simulated with signal to clutter ratios of 0, 10, and 20 dB. The clutter that was added to the anechoic lesion simulations was made using the multipath scattering approach described earlier. Approximately 8 diffuse clutter sites were added to the signal every 0.25 mm. The clutter sites could originate from anywhere shallow to the region where they would be added to the linear simulation and up to 1 cm on either side of the transmit beam's axis. Each diffuse clutter site contained 25 scatterers. ADMIRE was applied with the parameters in Table II.

### *I*. In Vivo Examples

We evaluated ADMIRE on three *in vivo* data sets acquired with a Siemens S2000 and 4C-1 curvilinear array (Siemens Healthcare, Ultrasound Business Unit, Mountain View, CA, USA). Two of the data cases were acquired at 4 MHz, and the third was a harmonic pulse inversion sequence with a 1.8-MHz transmit frequency and a 3.6-MHz center frequency on receive. ADMIRE was applied to the data as described in Table II. The model sampling parameters for the region of interest were $0.167\mathrm{res}_{\mathrm{lat}}$, $0.688\mathrm{res}_{\mathrm{axl}}$, and $0.0485\lambda$ for the lateral, axial, and phase dimensions, respectively. Outside the region of interest the sampling was $3.35\mathrm{res}_{\mathrm{lat}}$, $3.35\mathrm{res}_{\mathrm{axl}}$, and $0.2423\lambda$ for the lateral axial and phase dimensions, respectively. For comparison, the data sets were beamformed with and without hamming apodization on receive. Apodization was applied after ADMIRE.

# III. Results

## A. Model Error and Clutter Correlation Patterns

Model errors are shown in Fig. 4. The figure compares the model error for our previous model and two realizations of the current model. The region of interest is at 5 cm for the results shown in the figure. The current model is shown without an additional dynamic receive-based modulation and with an additional modulation. The results show that the error for the new model is similar regardless of the modulation, but the modulation does allow the region of interest to be decomposed with the lowest error predictors, and it increases the size of the region with error less than −20 dB. In addition to shifting the region of lowest model error, changing the modulation also expands the size of the zone where model error is below −20 dB. The model error for all the models becomes high in the very near-field, which may be related to the performance of Field II in the near-field.

## B. Example of a Simulated Cluttered Wavefront

We show an example of simulated cluttered data using the approach described in the methods in Fig. 5. The figure shows an uncluttered Field II simulation and the same Field II simulation cluttered with simulated multipath and off-axis scattering. The cluttered simulation contains qualitative features similar to the *in vivo* data, which includes sharp discontinuities across the aperture and apparent suppression of the wavefront in some regions. From visual inspection of the *in vivo* data, there are likely also sound-speed variation (i.e., phase-aberration) errors, which is not currently included in the simulation approach introduced here.

## C. Regularization Parameters

The results of varying $\alpha$ and $\lambda$ from (15) are shown in Fig. 6. These results demonstrate several important ideas about the ADMIRE model fit, and the advantages of incorporating an elastic-net scheme instead of solely L1 ($\alpha = 1$) or L2 ($\alpha = 0$) regularization. Figs. 6(a) and 6(c) show the decrease in the full signal error as a function of increasing degrees of freedom. (In this case plotting the independent axis using degrees of freedom instead of lambda more readily enables comparison between different values of $\alpha$, which are each optimized with different $\lambda$ values.) Displaying the data against degrees of freedom initially suggests that L1 produces the best fit with the smallest error for small degrees of freedom. This result is usually desirable; however, in this case L1 does not always produce the lowest error of the wavefront of interest, which is shown in Figs. 6(b) and 6(d). We also show that L1 does not produce the best improvement in contrast, which is shown in Figs. 6(f) and 6(h). The end result is that although L1 results in the best decomposition of the cluttered signal, L1 does not lead to the best decluttered image.

For the task of reconstructing the wavefront of interest L2 can achieve the lowest mean square error with the fewest degrees of freedom. However, although L2 reconstructs the signal shape well, L2 by itself fails to effectively reject sources of clutter originating outside the region of interest as demonstrated in Figs. 6(e), 6(g), 6(f), and 6(h).

Figs. 6(e) and 6(g) show the amount of energy in the signal of interest when the true signal is composed only of clutter sources (lower is better). This represents the scenario of a truly anechoic cyst. This is further emphasized in Figs. 6(f) and 6(h) showing the image contrast proxy, (21).

### D. Image Quality

Example lesions of the uncluttered linear contrast simulations are shown in Fig. 7. These results show good qualitative agreement without clutter. The summary statistics for the contrast simulations are displayed in Fig. 8. These results compare normal B-Mode versus B-Mode images formed from several different sets of regularization parameters. The contrast simulation results are summarized using contrast, CNR, and speckle SNR. The primary result is that ADMIRE preserves normal B-mode imaging metrics when clutter is not present, and in a few cases ADMIRE does better, such as with the anechoic contrast simulation. This is important because it demonstrates that ADMIRE does not degrade or otherwise corrupt high-quality B-mode data.

Example lesions of cluttered anechoic contrast simulations are shown in Fig. 9. These results provide an example of how the Field II multipath clutter image degradation looks for various signal to clutter levels. The summary statistics in Fig. 10 demonstrate that the ADMIRE images largely have better image metrics. The change in CNR is modest, but this small improvement in CNR may be correlated with the relatively high variance inside the lesion even after decluttering.

To demonstrate that the simulation results translate to *in vivo* data two examples are shown in Fig. 11 with contrast and CNR metrics compiled in Table III. Results are shown for several sets of regularization parameters. For each set of parameters, the contrast is clearly better compared with the original data, but in some cases the CNR decreases. However, based on the previous CNR results from Field II simulations and visual inspection of the *in vivo* example case shown in Fig. 11 it is reasonable to attribute the decrease in CNR to additional structure introduced in the background region used to calculate the image metrics. Similar levels of improvement are encountered when ADMIRE is applied to fundamental or harmonic data. We also report the full run time for each of the in vivo cases using $\alpha = 0.9$ and $\gamma = 0.5$ and operating on a single core of an Intel Core i7-4790 3.60 GHz processor (Intel Corporation, Santa Clara, CA, USA). The total serial run times for the fundamental cases were 46 932 s and 46 540 s. The harmonic run time was 27 542 s.

## IV. Discussion

We have presented a new model and decomposition approach for the ultrasound clutter problem, which we refer to as ADMIRE. ADMIRE solves many of the open questions from our previous method. These include preservation of image quality and decomposition issues. One significant question from before was how many model components to include in the final decomposition. This is now a function of the regularization constraints and can be tuned to maximize image quality. It should be noted that some of the image quality improvements are related to better STFT and ISTFT parameters compared with those

coupled to our previous algorithm, and therefore even the old model and decomposition scheme perform better than in the original implementation [30].

To support ADMIRE, a pseudo nonlinear modification to Field II was introduced. We presented a qualitative demonstration of this approach for generating realistic clutter, but the ultimate goal was to develop a useful tool for tuning the regularization parameters. To this end, the unique application of Field II to generate multipath scattering was successful at generating regularization parameters that translated successfully to both fundamental and harmonic *in vivo* data.

In our implementation of the model we assumed that a Gaussian envelope was a reasonable representation of the pulse shape. This assumption was not rigorously tested here, but qualitative inspection of the *in vivo* data does not reveal gross changes in the speckle pattern or the resolution between normal and decluttered B-mode images. Also, as mentioned previously, our algorithm is not dependent on the Gaussian pulse approximation, and if necessary future algorithms can implement more sophisticated approaches to better account for the pulse shape.

ADMIRE's biggest drawback is run time. The reported run times for the example cases are a few hours per frame, which is the serial run time for a Matlab (The Mathworks Inc., Natick, MA, USA) implementation. The algorithm itself is easily parallelized, but even with a massively parallel graphical processing unit (GPU) based implementation this would likely still require several seconds per frame. Moving forward, it will be important to consider computational or algorithmic modifications that can reduce processing time without sacrificing the demonstrated improvements.

While the improvements realized in the *in vivo* examples shown in Figs. 11 and 12 are compelling, the reduced clutter could lead viewers to inappropriately put diagnostic emphasis on clutter that is not eliminated. It is important to realize that the current implementation is only designed to act on reverberation and off-axis scattering distributed along the axial and lateral dimensions. Image degradation from other sources such as diffraction limitations, phase aberration, or clutter from out of the imaging plane are not addressed here. These mechanisms of degradation could be integrated into ADMIRE in the future.

Finally, it is important to mention that although we are decomposing the received signal into a specific set of scatterers, there are multiple distributions of scatterers that can recreate any given wavefront. The specific scatterers that end up in the final model fit are a function of the model space sampling and the choice of regularization parameters. Based on this, we do not assume that there is any connection between the nonzero coefficients from the model fit and the actual scatterers in the imaged media. We do assume that the collection of scatterers within a given region considered as a whole are representative of the actual wavefront returning from a given region of tissue.

## V. Conclusions

The problem of acoustic clutter is unresolved, and is still responsible for failed exams in many patients. To resolve this issue we proposed a new model-based approach, ADMIRE. The approach declutters and preserves the RF-channel data, which means it should be able to function in conjunction with other classic ultrasound algorithms. Our results show that ADMIRE preserves B-mode image quality and acts as an all-pass filter when clutter levels are minimal; however, as clutter levels increase ADMIRE effectively suppresses clutter energy, restoring image quality. Finally, it is worth noting that the final output is still a B-mode image, which is consistent with the training of current healthcare workers.

## Acknowledgments

The authors would like to thank N. Danieley and M. Palmeri for computer assistance, and the staff of the Vanderbilt University ACCRE computing resource. We would also like to thank the reviewers for their helpful comments and J. Dahl and M. Jakovljevic for insightful suggestions.

The authors would like to acknowledge National Institutes of Health grant 1S10RR026828.

## Biographies

**Brett Byram** received the B.S. degree in biomedical engineering and math from Vanderbilt University, Nashville, TN, in 2004. He received the Ph.D. degree in biomedical engineering from Duke University, Durham, NC, where he then stayed as a research assistant professor. In August 2013, Brett joined the Biomedical Engineering department at Vanderbilt University, Nashville, TN, as an assistant professor. He has spent time working in Jørgen Jensen's Center for Fast Ultrasound, Lyngby, Denmark, and also in Siemens Healthcare's ultrasound division, Mountain View, CA. He currently runs the Biomedical Elasticity and Acoustic Measurement (BEAM) Laboratory, where he and others in the lab pursue solutions to clinical problems using ultrasound. He is affiliated with the Vanderbilt Initiative in Surgery and Engineering (ViSE) and the Vanderbilt University Institute of Imaging Science (VUIIS). His research interests include beamforming, motion estimation, and other related signal processing and hardware development tasks.

**Kazuyuki Dei** was born and raised in Saitama, Japan. He received the B.S. degree in mechanical engineering from the University of California, Berkeley, CA, in 2000. He worked for Fujitsu Limited and Fujitsu Semiconductor America Inc. as an electrical design and development engineer for more than 12 years. He is currently pursuing the Ph.D. degree in biomedical engineering at Vanderbilt University. His current research interests are a model-based clutter suppression and phase-aberration measurements of ultrasonic signals.

**Jaime Tierney** received her B.A. degree in mathematics in 2012 from the College of the Holy Cross in Worcester, MA. She worked for two years as an Image Analyst at inviCRO, a medical imaging services and software company in Boston, MA. She is now pursuing a Ph.D. degree in biomedical engineering at Vanderbilt University in Nashville, TN. Her research interests include microvasculature perfusion estimation techniques using noninvasive ultrasound imaging.

**Douglas Dumont** received the B.S.E and Ph.D degrees in biomedical engineering from Duke University, Durham, NC. Since 2013, he has worked as a researcher in the Department of Biomedical Engineering at Vanderbilt University, Nashville, TN. His research interests include medical ultrasound, elasticity imaging, and ultrasonic signal and image processing.

## References


[1]. Smith-Bindman R, Miglioretti DL, Johnson E, Lee C, Feigelson HS, Flynn M, Greenlee RT, Kruger RL, Hornbrook MC, Roblin D, Solberg LI, Vanneman N, Weinmann S, Williams A. Use of diagnostic imaging studies and associated radiation exposure for patients enrolled in large integrated health care systems, 1996-2010. JAMA. 2012; 307(22):2400–2409. [PubMed: 22692172]

[2]. Flynn BC, Spellman J, Bodian C, Moitra VK. Inadequate visualization and reporting of ventricular function from transthoracic echocardiography after cardiac surgery. J. Cardiothorac. Vasc. Anesth. Apr; 2010 24(2):280–284. [PubMed: 19833534]

[3]. Heidenreich PA, Stainback RF, Redberg RF, Schiller NB, Cohen NH, Foster E. Transesophageal echocardiography predicts mortality in critically ill patients with unexplained hypotension. J. Am. Coll. Cardiol. Jul; 1995 26(1):152–158. [PubMed: 7797744]

[4]. Hendler I, Blackwell SC, Bujold E, Treadwell MC, Mittal P, Sokol RJ, Sorokin Y. Suboptimal second-trimester ultrasonographic visualization of the fetal heart in obese women: Should we repeat the examination? J. Ultrasound Med. Sep; 2005 24(9):1205–1209. [PubMed: 16123180]

[5]. Khoury FR, Ehrenberg HM, Mercer BM. The impact of maternal obesity on satisfactory detailed anatomic ultrasound image acquisition. J. Matern.-Fetal Neonat. Med. Apr; 2009 22(4):337–341.

[6]. Kurt M, Shaikh KA, Peterson L, Kurrelmeyer KM, Shah G, Nagueh SF, Fromm R, Quinones MA, Zoghbi WA. Impact of contrast echocardiography on evaluation of ventricular function and clinical management in a large prospective cohort. J. Am. Coll. Cardiol. Mar; 2009 53(9):802–810. [PubMed: 19245974]

[7]. Pinton GF, Trahey GE, Dahl JJ. Erratum: Sources of image degradation in fundamental and harmonic ultrasound imaging: A nonlinear, full-wave, simulation study. IEEE Trans. Ultrason. Ferroelectr. Freq. Control. Jun; 2011 58(6):1272–1283. [PubMed: 21693410]

[8]. Flax SW, O'Donnell M. Phase-aberration correction using signals from point reflectors and diffuse scatterers: Basic principles. IEEE Trans. Ultrason. Ferroelectr. Freq. Control. Jan; 1988 35(6): 758–767. [PubMed: 18290213]

[9]. Krishnan S, Li P-C, O'Donnell M. Adaptive compensation of phase and magnitude aberrations. IEEE Trans. Ultrason. Ferroelectr. Freq. Control. 1996; 43(1):44–55.

[10]. Liu DL, Waag RC. Correction of ultrasonic wavefront distortion using backpropagation and a reference waveform method for time-shift compensation. J. Acoust. Soc. Am. Aug; 1994 96(2, pt. 1):649–660. [PubMed: 7930065]

[11]. Seo CH, Yen JT. Sidelobe suppression in ultrasound imaging using dual apodization with cross-correlation. IEEE Trans. Ultrason. Ferroelectr. Freq. Control. Oct; 2008 55(10):2198–2210. [PubMed: 18986868]

[12]. Guenther DA, Walker WF. Robust finite impulse response beamforming applied to medical ultrasound. IEEE Trans. Ultrason. Ferroelectr. Freq. Control. Jun; 2009 56(6):1168–1188. [PubMed: 19574125]

[13]. Holfort IK, Gran F, Jensen JA. Broadband minimum variance beamforming for ultrasound imaging. IEEE Trans. Ultrason. Ferroelectr. Freq. Control. Feb; 2009 56(2):314–325. [PubMed: 19251518]

[14]. Synnevag J-F, Austeng A, Holm S. Adaptive beamforming applied to medical ultrasound imaging. IEEE Trans. Ultrason. Ferroelectr. Freq. Control. Aug; 2007 54(8):1606–1613. [PubMed: 17703664]

[15]. Wang Z, Li J, Wu R. Time-delay- and time-reversal-based robust Capon beamformers for ultrasound imaging. IEEE Trans. Med. Imaging. Oct; 2005 24(10):1308–1322. [PubMed: 16229417]

[16]. Ma Q, Ma Y, Gong X, Zhang D. Improvement of tissue harmonic imaging using the pulse-inversion technique. Ultrasound Med. Biol. Jul; 2005 31(7):889–894. [PubMed: 15972194]

[17]. Becher H, Tiemann K, Schlosser T, Pohl C, Nanda NC, Averkiou M. a. Powers J, Lüderitz B. Improvement in endocardial border delineation using tissue harmonic imaging. Echocardiography. Jul; 1998 15(5):511–518. [PubMed: 11175074]

[18]. Spencer K, Bednarz J, Rafter P, Korcarz C, Lang R. Use of harmonic imaging without echocardiographic contrast to improve two-dimensional image quality. Am. J. Cardiol. Sep; 1998 82(6):794–799. [PubMed: 9761093]

[19]. Rau JM, Måsøy S-E, Hansen R, Angelsen B, Tangen TA. Methods for reverberation suppression utilizing dual frequency band imaging. J. Acoust. Soc. Am. Sep; 2013 134(3):2313–2325. [PubMed: 23967962]

[20]. Fink M. Time reversal of ultrasonic fields—Part I: Basic principles. IEEE Trans. Ultrason. Ferroelectr. Freq. Control. 1992; 39(5):555–566. [PubMed: 18267667]

[21]. Osmanski B, Montaldo G, Tanter M, Fink M. Aberration correction by time reversal of moving speckle noise. IEEE Trans. Ultrason. Ferroelectr. Freq. Control. 2012; 59(7):1575–1583. [PubMed: 22828852]

[22]. Tanter M, Thomas J.-l. Fink M. Focusing and steering through absorbing and aberrating layers: Application to ultrasonic propagation through the skull. J. Acoust. Soc. Am. 1998; 103(5 Pt 1): 2403–2410. [PubMed: 9604342]

[23]. Hansen R, Måsøy S-E, Johansen TF, Angelsen BA. Utilizing dual frequency band transmit pulse complexes in medical ultrasound imaging. J. Acoust. Soc. Am. Jan; 2010 127(1):579–587. [PubMed: 20059003]

[24]. Näsholm SP, Hansen R, Måsøy S-E, Johansen TF, Angelsen BA. Transmit beams adapted to reverberation noise suppression using dual-frequency SURF imaging. IEEE Trans. Ultrason. Ferroelectr. Freq. Control. Oct; 2009 56(10):2124–2133. [PubMed: 19942500]

[25]. Näsholm SP, Hansen R, Angelsen B. Post-processing enhancement of reverberation-noise suppression in dual frequency SURF imaging. IEEE Trans. Ultrason. Ferroelectr. Freq. Control. 2011; 58(2):338–348. [PubMed: 21342819]

[26]. Dahl J, Jakovljevic M, Pinton GF, Trahey GE. Harmonic spatial coherence imaging: An ultrasonic imaging method based on backscatter coherence. IEEE Trans. Ultrason. Ferroelectr. Freq. Control. Apr; 2012 59(4):648–659. [PubMed: 22547276]

[27]. Jakovljevic M, Trahey GE, Nelson RC, Dahl JJ. In vivo application of short-lag spatial coherence imaging in human liver. Ultrasound Med. Biol. Mar; 2013 39(3):534–542. [PubMed: 23347642]

[28]. Camacho J, Parrilla M, Fritsch C. Phase coherence imaging. IEEE Trans. Ultrason. Ferroelectr. Freq. Control. May; 2009 56(5):958–974. [PubMed: 19473914]

[29]. Lediju MA, Trahey GE, Byram BC, Dahl JJ. Short-lag spatial coherence of backscattered echoes: Imaging characteristics. IEEE Trans. Ultrason. Ferroelectr. Freq. Control. Jul; 2011 58(7):1377–1388. [PubMed: 21768022]

[30]. Byram B, Jakovljevic M. Ultrasonic multipath and beam-forming clutter reduction: A chirp model approach. IEEE Trans. Ultrason. Ferroelectr. Freq. Control. Mar; 2014 61(3):428–440. [PubMed: 24569248]

[31]. Kay, SM. Fundamentals of Statistical Signal Processing: Estimation Theory. Prentice-Hall Inc.; Upper Saddle River, NJ, USA: 1993.

[32]. Wagner RF, Smith SW, Sandrik JM, Lopez H. Statistics of speckle in ultrasound B-scans. IEEE Trans. Sonics Ultrason. 1983; 30:156–163.

[33]. Selfridge AR, Kino GS, Khuri-Yakub BT. A theory for the radiation pattern of a narrow-strip acoustic transducer. Appl. Phys. Lett. 1980; 37(1):35.

[34]. Lv X, Bi G, Wan C, Xing M. Lv's distribution: Principle, implementation, properties, and performance. IEEE Trans. Signal Process. 2011; 59(8):3576–3591.

[35]. Zou H, Hastie T. Regularization and variable selection via the elastic net. J. R. Stat. Soc. Series B Stat. Methodol. Apr; 2005 67(2):301–320.

[36]. Friedman J, Hastie T, Tibshirani R. Regularization paths for generalized linear models via coordinate descent. J. Stat. Softw. 2010; 33(1):1–22. [PubMed: 20808728]

[37]. Tibshirani RJ, Taylor J. Degrees of freedom in lasso problems. Ann. Stat. Apr; 2012 40(2):1198–1232.

[38]. Liu X, Wen Z, Zhang Y. Limited memory block krylov subspace optimization for computing dominant singular value decompositions. SIAM J. Sci. Comput. 2013; 35(3):A1641–A1668.

[39]. Yang, B. A study of inverse short-time Fourier transform; IEEE Int. Conf. Acoustics, Speech and Signal Processing; 2008; p. 3541-3544.

[40]. Jensen JA. A model for the propagation and scattering of ultrasound in tissue. J. Acoust. Soc. Am. Jan; 1991 89(1):182–190. [PubMed: 2002167]

[41]. Jensen JA, Svendsen NB. Calculation of pressure fields from arbitrarily shaped, apodized, and excited ultrasound transducers. IEEE Trans. Ultrason. Ferroelectr. Freq. Control. 1992; 39:262–267. [PubMed: 18263145]

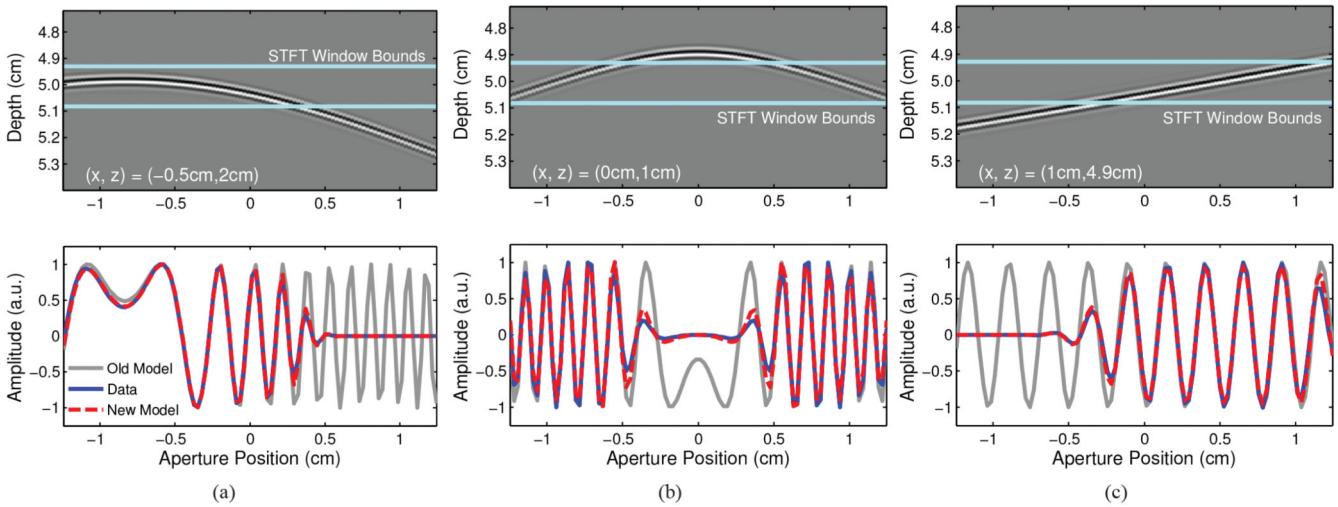


**Fig. 1.**

Three examples are shown for the time-domain channel data and the corresponding aperture domain data after the STFT has been applied axially. The examples show several cases of $x_n$, $z_n$, and $\tau_n$ for a region of interest centered about 5 cm. Comparisons are made between the data, the new model, and the old model in each of the bottom graphs.

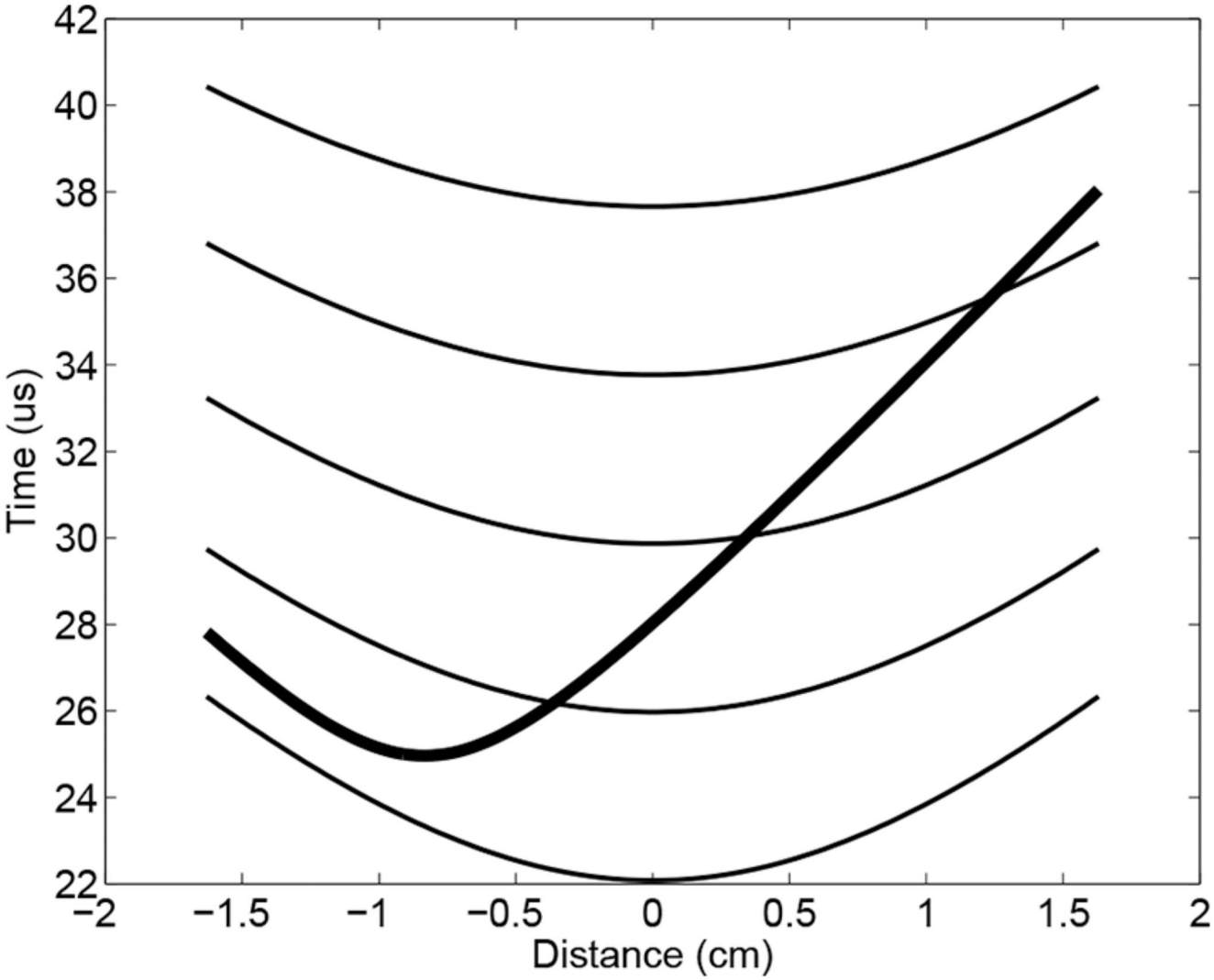


**Fig. 2.**

When multipath scattering does occur, the wavefront will extend across multiple dynamic receive delay profiles. This is demonstrated in the graph above with several receive delay profiles shown as thin lines, and a wavefront delay profile from modeled multipath scattering shown as a black line.

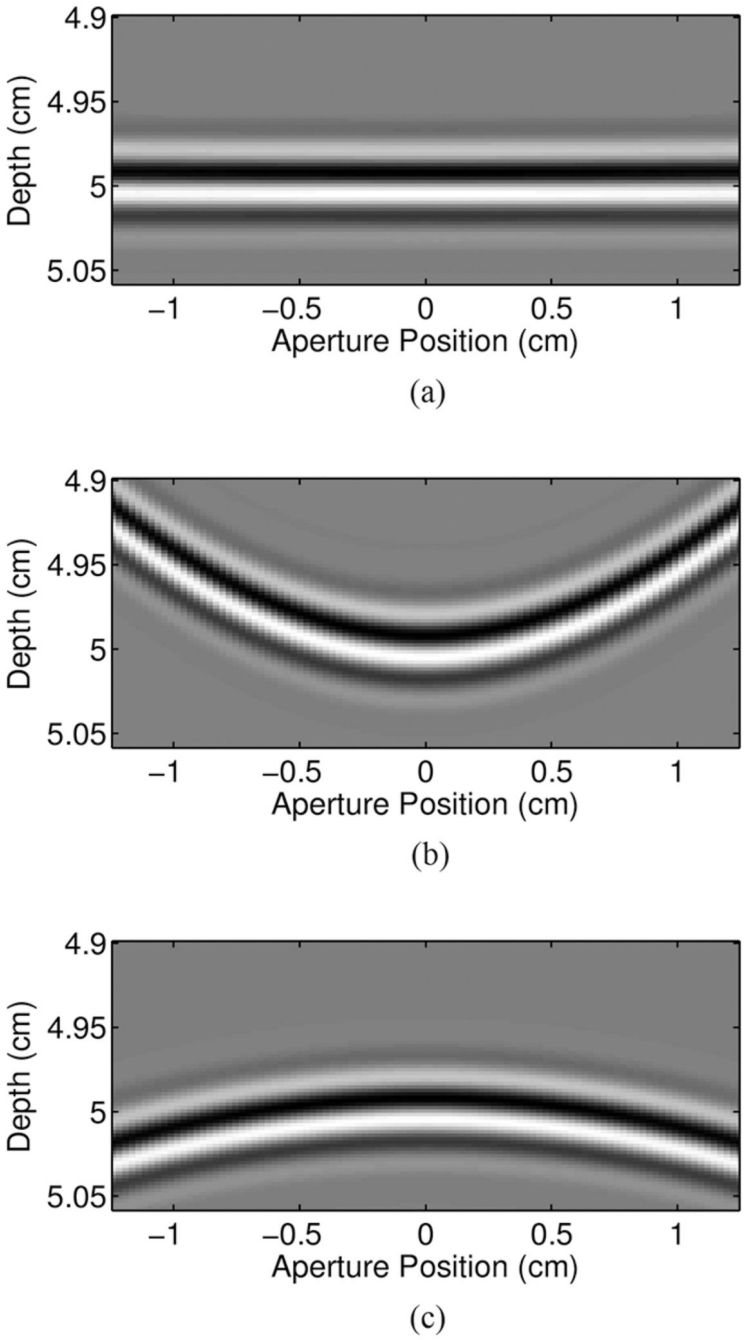


**Fig. 3.**

Three examples are shown for different dynamic receive $\gamma$ scales. When $\gamma$ is negative, the dynamic receive foci are shallower than normal so the wavefront becomes inverted, and when $\gamma$ is positive the curvature from path-length differences is not entirely removed so some of the original curvature remains. (a) $\gamma = 0$, (b) $\gamma = -0.5$, (c) $\gamma = 0.5$.

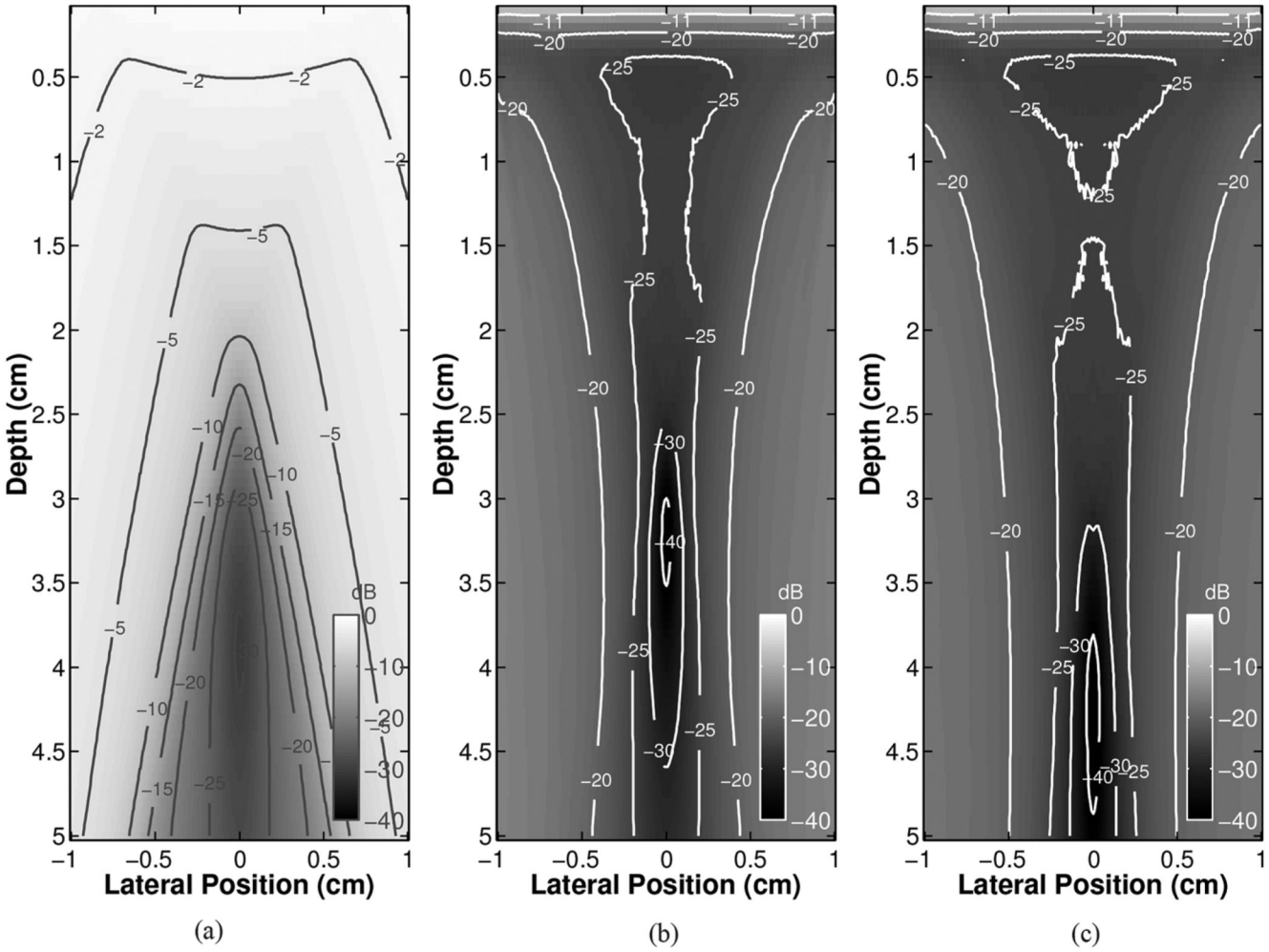


**Fig. 4.**

Model error power is shown for the old model (a), the proposed model without additional modulation (b), and the new model with an additional modulation corresponding to $\gamma = 0.5$ (c). The new model has distinctly lower model error compared with the old model. The new model has low error for both cases, but the case of the intentional receive modulation has slightly lower error.

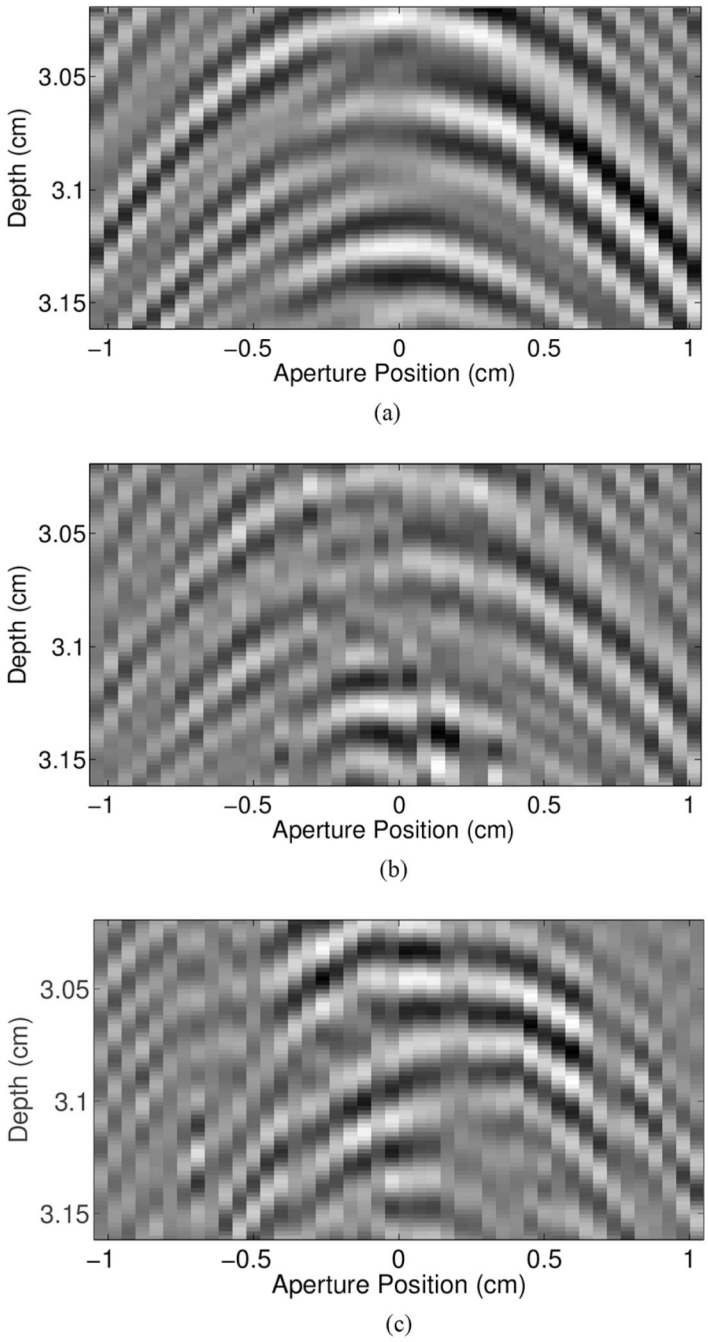


**Fig. 5.**

An example of the multipath Field II simulations is shown. In (a), a normal Field II simulation is shown. In (b), the same Field II simulation corrupted by Field II simulated multipath scattering is shown. In (c), an *in vivo* example featuring several distinct wavefronts is shown. The Field II simulation with simulated multipath and off-axis clutter features some similarities to the *in vivo* data that are not present in the usual Field II simulation. For example, in the *in vivo* and cluttered simulation, there are apparent sharp discontinuities in the wavefront that are not apparent in the first Field II simulation.

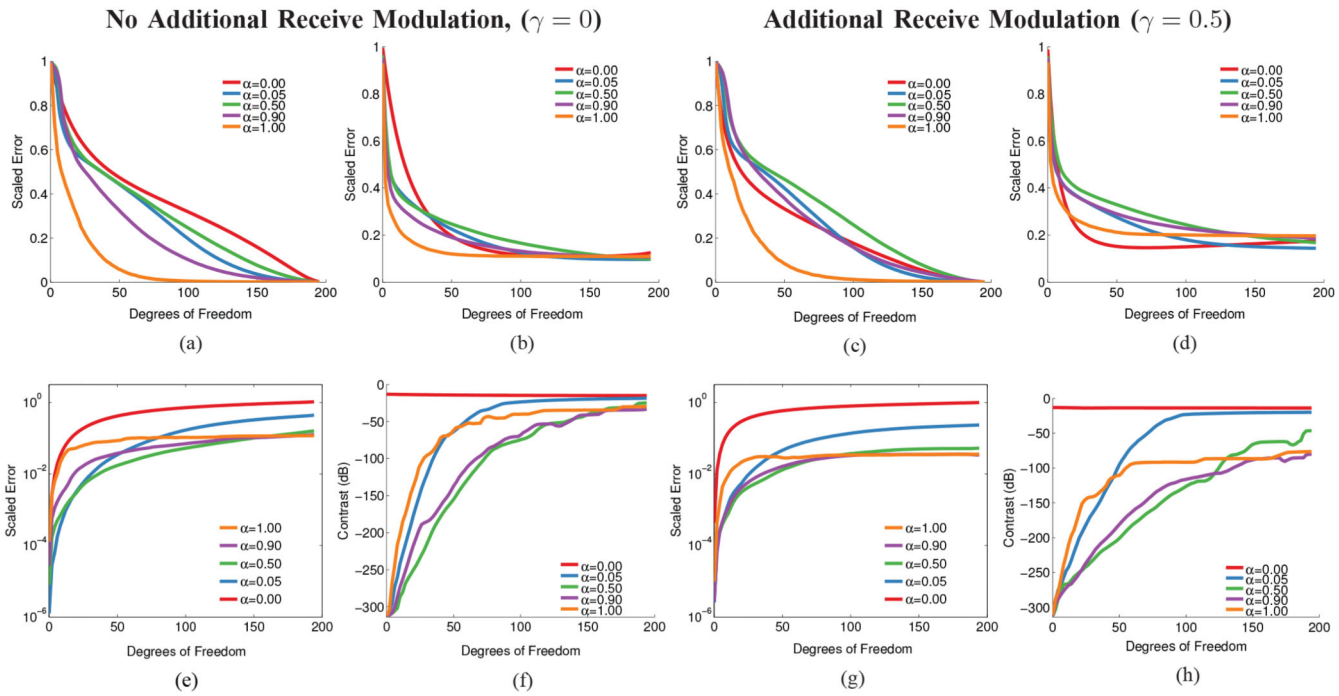


**Fig. 6.**

Several different errors are shown as a function of degrees of freedom for several values of $a$ between L1 (lasso regression) and L2 (ridge regression) regularized model fits. Figs. 6(a) and 6(c) imply that L1 is the best scheme for minimizing the error of the complete aperture domain signal; however, Figs. 6(b) and 6(d) demonstrate that L2 produces the lowest error for the wavefront returning from the region of interest. These results are mitigated by the results in Figs. 6(e), 6(g), 6(f), and 6(h), which demonstrate that an $a$ value between 0 and 1 performs better at suppressing signals outside the region of interest and adequately reconstructing the wavefront originating from the region of interest. (a) Complete signal error, (b) region of interest error, (c) complete signal error, (d) region of interest error, (e) region of interest without signal, (f) contrast, (g) region of interest without signal, (h) contrast.

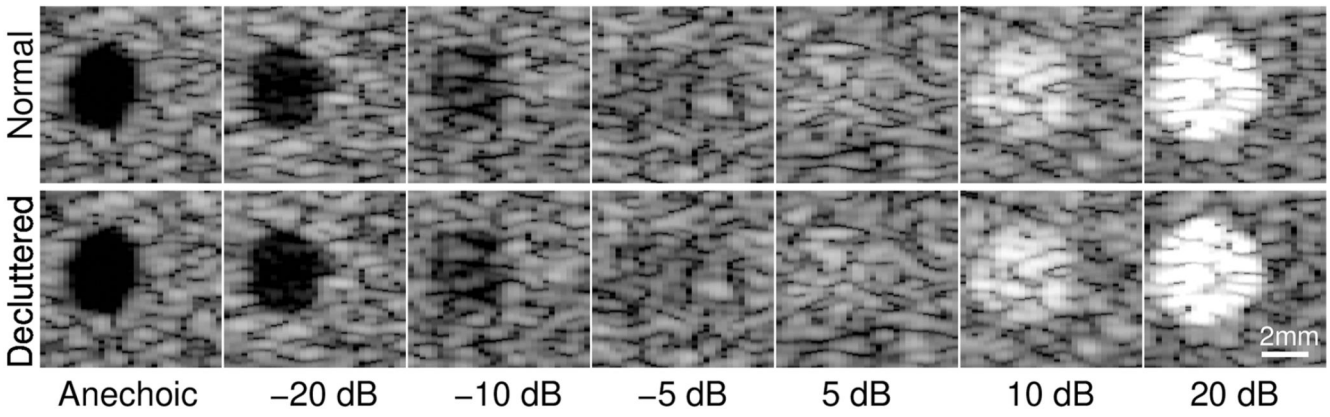


**Fig. 7.**

4-mm lesions are visualized using a 3-MHz F/2 imaging system. The contrast of the simulated phantoms goes from completely anechoic to +20 dB. For all cases there is little change between the decluttered and normal B-mode data. The full summary of all the simulations is shown in Fig. 8, but the result is that the decluttering algorithm does not produce images with worse image metrics in the absence of clutter.

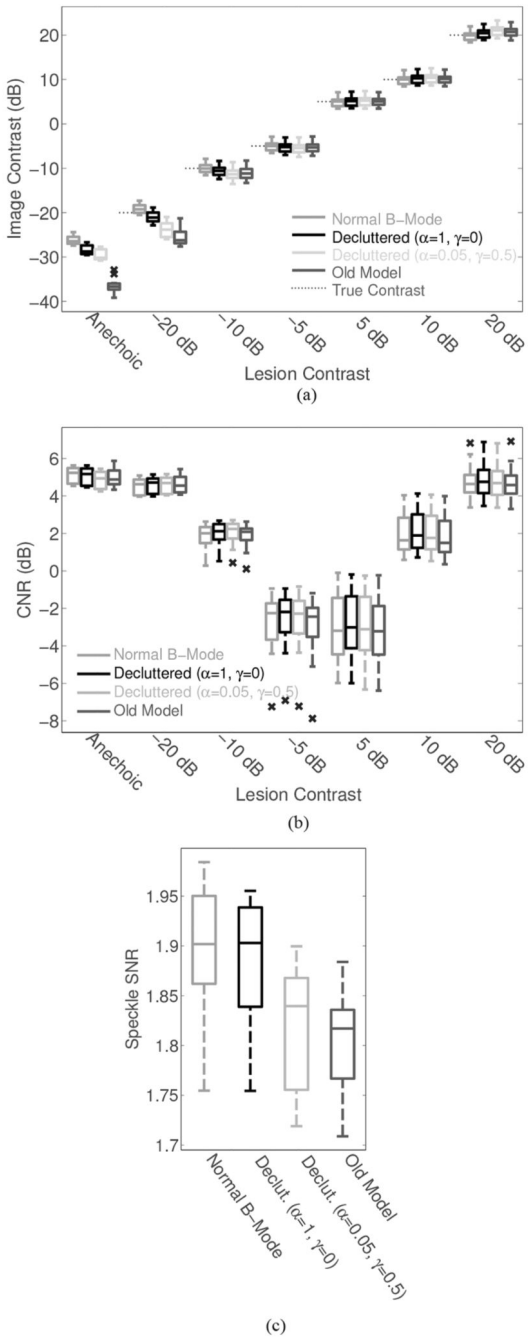


**Fig. 8.**

The results of 12 speckle realizations are shown as boxplots for several levels of lesion contrast and CNR. Results are also shown for speckle SNR. Results are shown for normal B-mode, and the new and old models. In these results, the shortcomings of the old model are clearly evident in the CNR and speckle SNR data, but in contrast the new model does not have worse CNR or speckle SNR than normal B-mode imaging. In some instances, the CNR may be slightly better compared with B-mode imaging. (a) Contrast, (b) CNR, (c) speckle SNR.

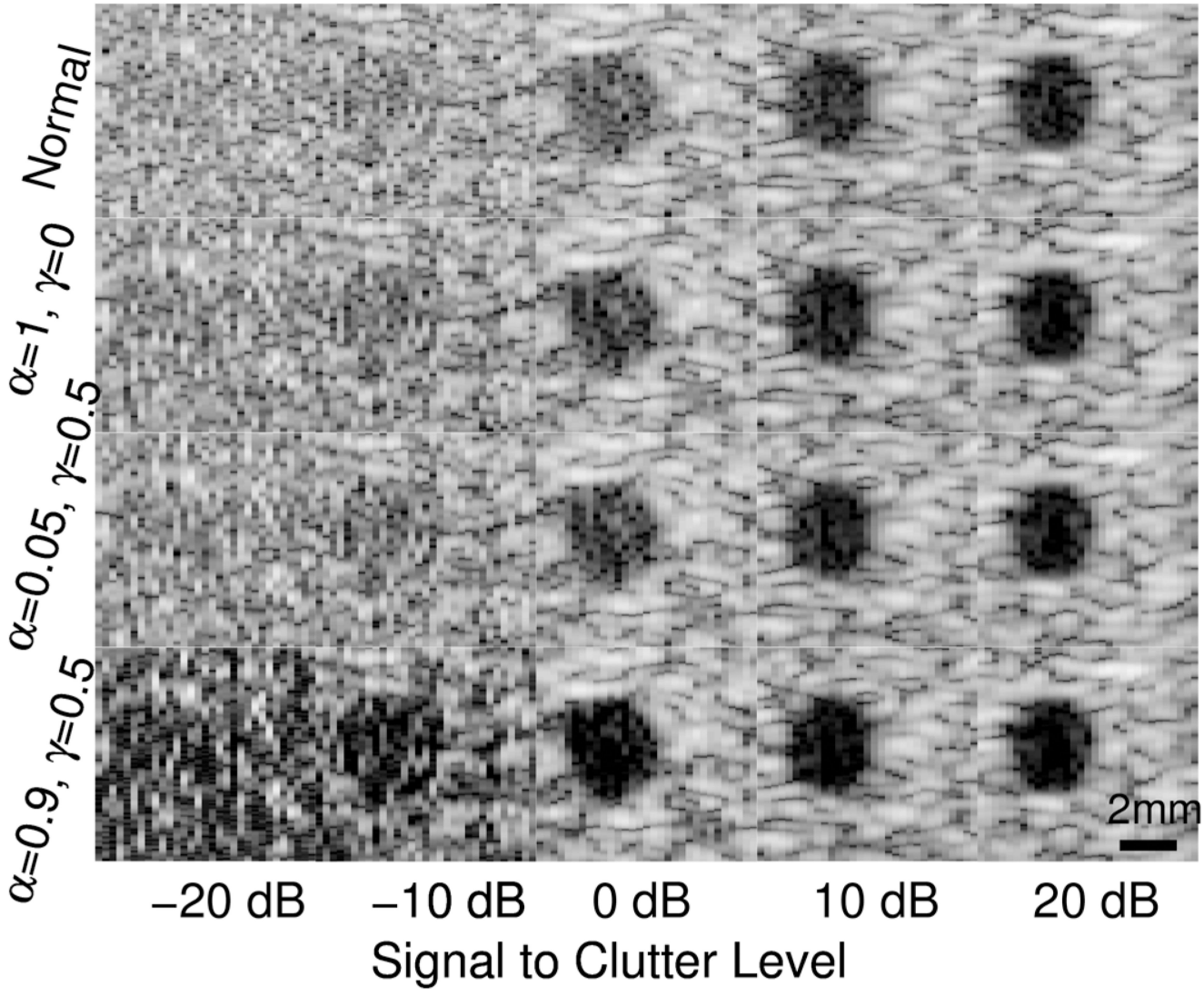


**Fig. 9.**

4-mm lesions are visualized using a 3-MHz F/2 imaging system. The contrast of the simulated phantoms goes from completely anechoic to +20 dB. For all cases there is little change between the decluttered and normal B-mode data. The full summary of all the simulations is shown in Fig. 10, but the result is that ADMIRE does not produce images with worse image metrics in the absence of clutter.

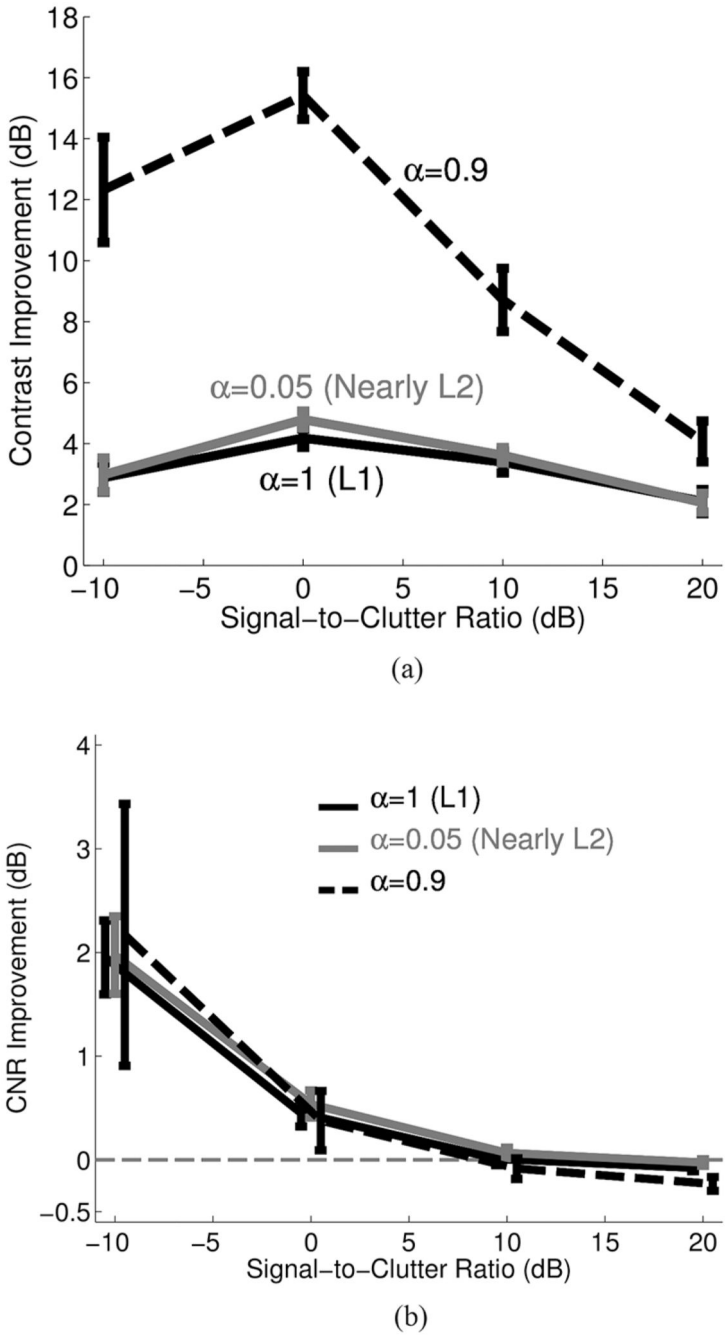


**Fig. 10.**

The results of cluttered anechoic lesion simulations are shown as boxplots for several levels of signal-to-clutter ratio. (a) Contrast, (b) contrast-to-noise ratio. Results are shown for several different sets of regularization parameters. The results mostly show that ADMIRE images are better, but with very high or very low levels of signal-to-clutter ratio, the improvement is not substantial. The largest improvement are seen from the images formed using $\alpha = 0.9$ and $\gamma = 0.5$.

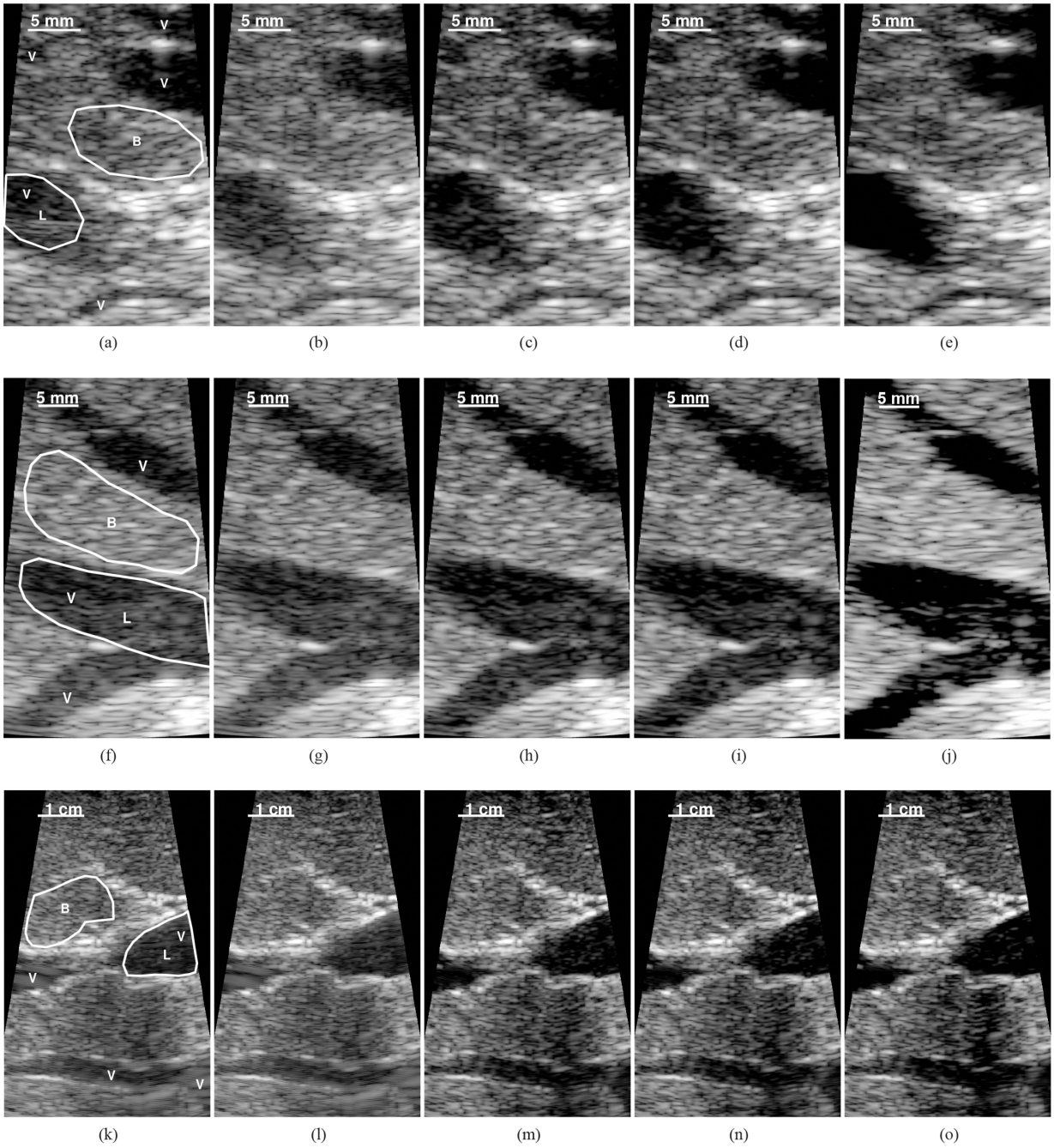


**Fig. 11.**

Two *in vivo* examples are shown to demonstrate that ADMIRE translates to clinical data. The results are qualitatively promising, and quantitative image metrics presented in Table III support the qualitative improvements. Hypoechoic regions of the image presumed to be vessels are indicated with V, and the regions used to calculate image metrics are outlined and denoted with an L or B indicating lesion or background, respectively. In both cases, image improvements in the large structures are clear. In the first example, there is evidence that previously unvisualizable vessels (upper left corner) become visible after

decomposition. (a) Mask regions, (b) normal B-mode, (c) $\alpha = 1$, $\gamma = 0$, (d) $\alpha = 0.9$, $\gamma = 0$, (e) $\alpha = 0.9$, $\gamma = 0.5$, (f) mask regions, (g) normal B-mode, (h) $\alpha = 1$, $\gamma = 0$, (i) $\alpha = 0.9$, $\gamma = 0$, (j) $\alpha = 0.9$, $\gamma = 0.5$, (k) mask regions, (l) harmonic B-mode, (m) $\alpha = 1$, $\gamma = 0$, (n) $\alpha = 0.9$, $\gamma = 0$, (o) $\alpha = 0.9$, $\gamma = 0.5$.

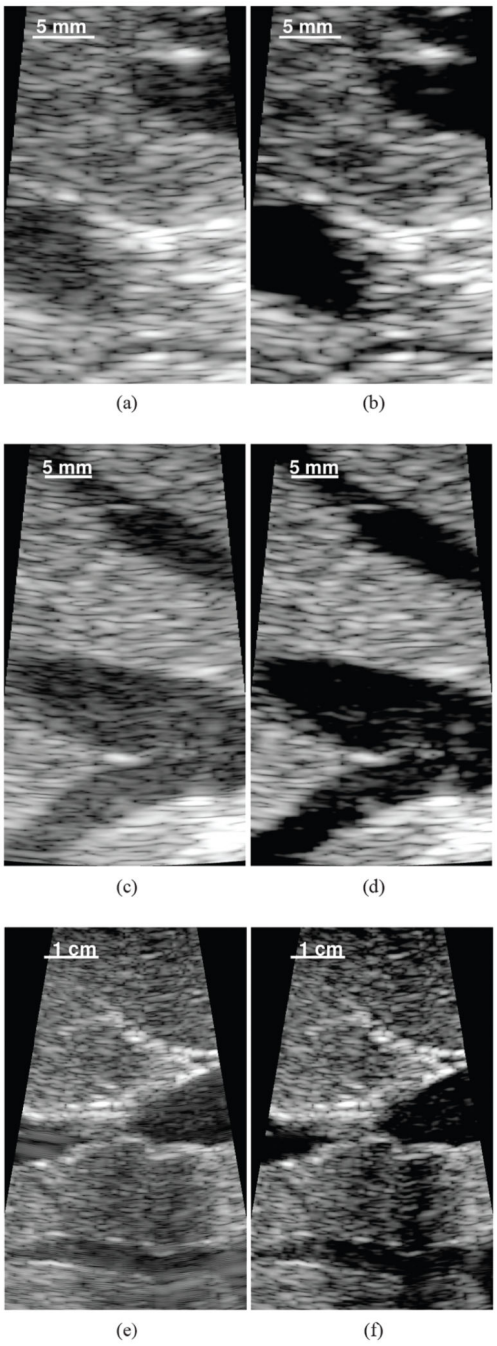


**Fig. 12.**

The effect of applying a hamming apodization window on receive is shown on the fundamental and harmonic B-mode images and the corresponding data after ADMIRE with the $\alpha = 0.9$ and $\gamma = 0.5$ case. The *in vivo* examples show that apodization only results in modest improvements compared with ADMIRE. The matched contrast and CNR results are shown in Table III. (a) Normal B-mode, (b) $\alpha = 0.9$, $\gamma = 0.5$, (c) normal B-mode, (d) $\alpha = 0.9$, $\gamma = 0.5$, (e) harmonic B-mode, (f) $\alpha = 0.9$, $\gamma = 0.5$.

**TABLE I**

**Field II Simulation Parameters**

| Parameter | Value |
|---|---|
| Center frequency ($f_c$) | 3 MHz |
| Bandwidth | 60% |
| Lateral pitch | 0.257 mm |
| Elevation width | 2 mm |
| Samp. freq. (simulation) | 640 MHz |
| Samp. freq. (downsampled) | 40 MHz |
| Transmit focal depth | 3 cm |
| Transmit f-number | 1.8 |
| Receive f-number | 2 |
| Lesion radius | 2 mm |
| Lesion center depth | 3 cm |

**TABLE II**

**Decomposition Parameters**

| Parameter | Value |
|---|---|
| STFT window length | $(8\log(2))/(2\pi \mathrm{BW} f_0)$ |
| STFT padded window length | 2 × window length |
| STFT window type | Rectangular |
| STFT window overlap | 90% |
| Decomposed bandwidth | 120% |
| $c_l$ | 6 |
| $c_a$ | 2 |
| $\gamma$ | Variable |
| $\alpha$ | Variable |
| $\lambda$ | Variable |
| Sampling grid | Variable |

**TABLE III**

***In Vivo* Image Metrics**

| | Contrast (dB) | | CNR (dB) | |
|---|---|---|---|---|
| **Parameters** | **Rect.** | **Hamm.** | **Rect.** | **Hamm.** |
| Case #1 (fundamental) | | | | |
| Normal B-mode | 12.4 | 13.1 | 0.76 | 0.49 |
| $\alpha = 1, \gamma = 0$ | 17.6 | 19.9 | 0.17 | 0.30 |
| $\alpha = 0.9, \gamma = 0$ | 20.9 | 23.6 | 0.50 | 0.61 |
| $\alpha = 0.9, \gamma = 0.5$ | 37.2 | 41.2 | 1.38 | 0.64 |
| Case #2 (fundamental) | | | | |
| Normal B-mode | 13.9 | 14.3 | 1.28 | 1.70 |
| $\alpha = 1, \gamma = 0$ | 17.8 | 18.3 | 1.40 | 1.98 |
| $\alpha = 0.9, \gamma = 0$ | 18.5 | 19.1 | 1.48 | 2.10 |
| $\alpha = 0.9, \gamma = 0.5$ | 24.7 | 25.1 | 2.06 | 2.30 |
| Case #3 (harmonic) | | | | |
| Normal B-mode | 12.2 | 12.6 | −1.15 | −0.95 |
| $\alpha = 1, \gamma = 0$ | 19.0 | 19.2 | −0.47 | −0.42 |
| $\alpha = 0.9, \gamma = 0$ | 19.8 | 20.0 | −0.35 | −0.29 |
| $\alpha = 0.9, \gamma = 0.5$ | 24.0 | 24.7 | 0.05 | 0.10 |